




# Two-dimensional hierarchical porous carbons with mesopore-enriched architectures for high-reactivity and stable lithium-ion full batteries

Shilin Yun<sup>1</sup>, Zhiqiang Zhang<sup>1</sup>, Zhiwei Peng<sup>1</sup>, Chun Yang<sup>1</sup>, Rui Liu<sup>1</sup>, Yanxin Liao<sup>1</sup>, and Hai-Chao Chen<sup>1,\*</sup> 

<sup>1</sup>Institute of Materials for Energy and Environment, School of Materials Science and Engineering, Qingdao University, Qingdao 266071, China

**Received:** 19 October 2021

**Accepted:** 28 January 2022

**Published online:**  
15 February 2022

© The Author(s), under exclusive licence to Springer Science+Business Media, LLC, part of Springer Nature 2022

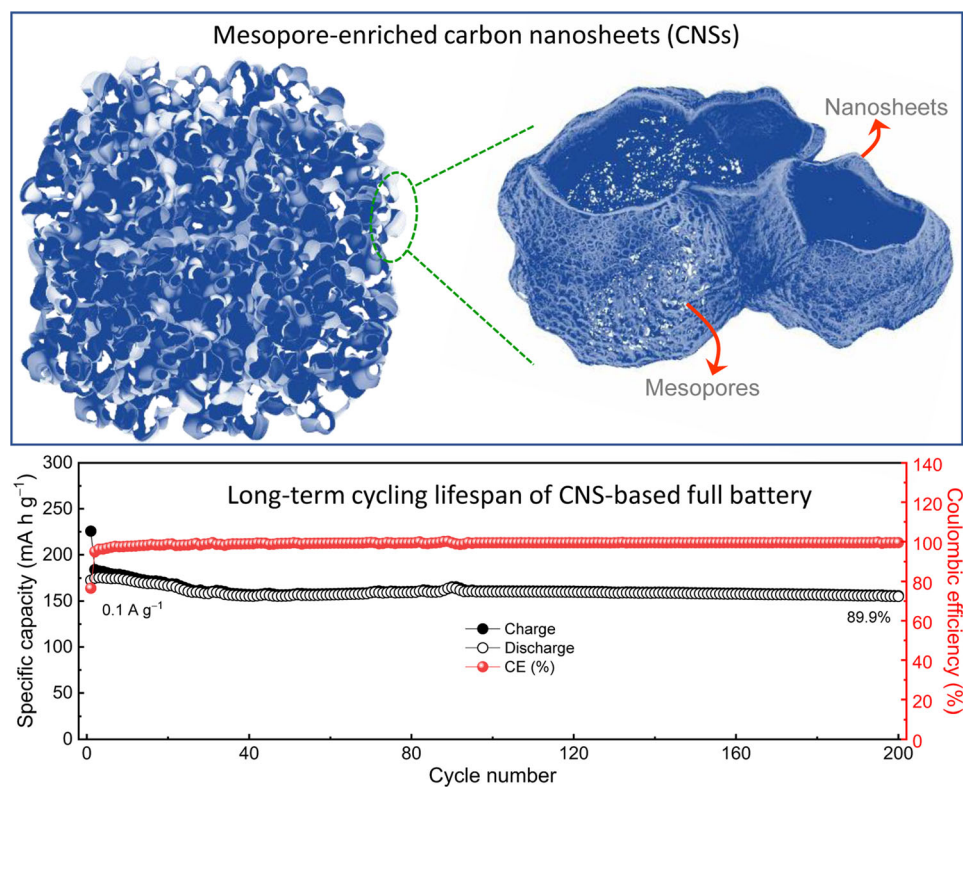
## ABSTRACT

Limited theoretical capacity of graphite anode and sluggish reaction kinetics of bulk electrodes are significant obstacles for achieving both high-energy and high-power performances of Li-ion batteries (LIBs). Here, the reduced dimension of porous carbon is used to lower the Li<sup>+</sup> diffusion distance, while the pore size is tuned to enhance the utilization efficiency for energy storage. The mesopore-enriched hierarchical porous carbon nanosheets (CNSs) are synthesized by direct pyrolysis of potassium citrate. Templating effect of potassium salt results in a 2D structure and its activation effect constructs a highly porous architecture. The pore sizes enhance with the increase of annealing temperature while a hierarchical porous architecture enriched with mesopores can be formed at 950 °C (CNS-950). The specific 2D structure and mesoporous architecture can increase the active sites and shorten ion diffusion distance, endowing CNSs with high-reactivity and fast reaction kinetics in LIB anode. The CNS-950 obtains a reversible capacity three times the theoretical capacity of graphite, and significant cyclic stability can be realized with a specific capacity of 1154 mA h g<sup>-1</sup> at 0.3 A g<sup>-1</sup> retained after 200 cycles. What's more, the electrode displays a capacity of 600 mA h g<sup>-1</sup> at a high current of 2 A g<sup>-1</sup>. The CNS-950 is used for the construction of full batteries which demonstrates a maximal energy/power density of 319 W h kg<sup>-1</sup>/2.9 kW kg<sup>-1</sup> and long-term cycling stability.

Handling Editor: Mark Bissett.

Address correspondence to E-mail: chenhc@qdu.edu.cn

## GRAPHICAL ABSTRACT



## Introduction

Lithium-ion batteries (LIBs) have been widely used as the energy supply for portable electronic devices and electronic vehicles owing to their wide operating potential, high-energy density and environmental friendliness [1–4]. Carbon-based materials are considered as the leading active material for anodes of commercial LIBs owing to their superiorities of low cost, high electrical conductivity, good chemical stability, and environmental friendliness [5–7]. However, the most common graphite anode has a limited theoretical capacity of 372 mA h g<sup>-1</sup>, and the capacity realized by commercialized graphitic carbons close to this level, making the maximum energy density of commercialized LIBs restricted to approximate 120–200 W h kg<sup>-1</sup> without further advancement in recent years. In addition, bulk ion diffusion in the 2D tunnel structure of graphitic

carbon results in slow diffusion kinetics and thus poor power density (< 1 kW kg<sup>-1</sup>). Based on these considerations, plentiful of alternative carbon anodes such as activated carbon (AC) [8], ordered mesoporous carbon [9], hierarchically porous carbon [10], graphene [11, 12], etc., have been developed with exciting results.

Porous carbons are typical carbon materials with attractive merits of high electron conductivity, large surface area, well-developed porosity, and so on. Their energy storage achieved by surface-related Li-ion adsorption, intercalation, or deposition with a fast reaction kinetics, and large surface area endowed by highly porous structure contributes to a capacity 2–3 times that of graphitic carbon [9, 13–15]. Besides their applications in LIBs, different porous carbons are reported for applications in fields of supercapacitors [16, 17], Na-ion battery [18], K-ion battery [19, 20], microwave absorption [21, 22], CO<sub>2</sub> adsorption [23], etc. Traditionally, microporous carbon is prepared as

granular particles larger than 10  $\mu\text{m}$ , and its tortuous and narrow pores severely limit the kinetics for ion transfer. The following two strategies can be adopted to increase the effective diffusion path for  $\text{Li}^+$ . The first strategy is to reduce the overall dimensions of carbon to a 0D, 1D or 2D size [24–26], which can significantly shorten ion diffusion distance ( $< 100\text{ nm}$ ). Another strategy is to combine large pores with micropores [10, 14, 16, 18, 27], whilst large pores can serve as both ion buffer reservoirs and fast transfer channels. Graphene is a good example of a 2D carbon; however, self-aggregation of graphene reduces the active surface and slows down the transfer rates of Li-ions. On the contrary, 2D porous carbons constitute a better alternative because they are easily prepared, and their unique 2D structure provides a short diffusion pathway for Li-ions [24, 26, 28]. Despite enhanced rate performance reported in anterior works, their specific capacity is still limited by their microporous porosity owing to the fact that micropores seem too narrow for Li-ion storage [24, 29–31]. In addition, these reports need a multi-step process for 2D porous carbon synthesis [25, 31–33], which is time-consuming and produces additional cost. Therefore, developing robust methods for carbon nanosheets with tunable porous sizes and high specific areas are still very crucial.

In this study, we report the successful fabrication of 2D carbon nanosheets (CNSs) with hierarchical micropores and mesopores via direct pyrolysis of potassium citrate. Templating effect of potassium salt results in a 2D structure and its activation effect constructs a highly porous architecture. By tuning the annealing temperature to 950  $^{\circ}\text{C}$ , our CNSs show a hierarchical porous architecture with enriched mesopores and large pore volume (CNS-950). The specific 2D structure increases the active sites and shortens the ion diffusion distance of CNSs, and mesoporous architecture further increases the reactivity and reaction kinetics for Li-ion storage. The CNS-950 shows the highest specific capacity with a reversible capacity three times the theoretical capacity of graphite can be achieved. Meanwhile, both high-rate and long-term cycling stability can be realized. The CNS-950-based full batteries also demonstrate excellent performance in terms of high-energy, high-power, and long-term cycling performances.

## Experimental

### Preparation of the CNSs

In a typical procedure, 5 g of potassium citrate was heat-treated in a tube furnace in Ar gas for 1 h with a heating rate of 3  $^{\circ}\text{C min}^{-1}$ . The pyrolysis temperatures are 850, 900 and 1000  $^{\circ}\text{C}$ , and the resultant samples were labeled CNS- $T$ , where  $T$  represents the annealing temperature. The product was washed with dilute hydrochloric acid and plenty of deionized water, and then, dried at 60  $^{\circ}\text{C}$ .

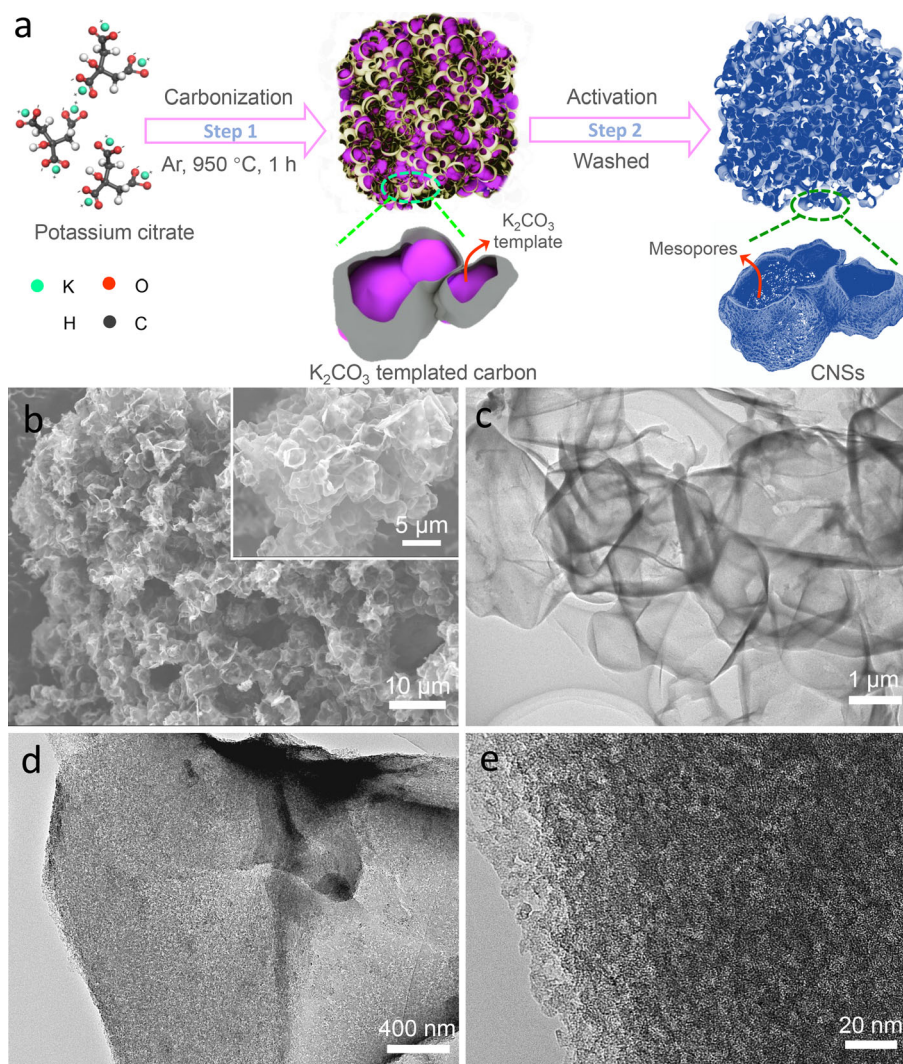
Materials characterization and electrochemical measurements can be found in *Supplementary Material*.

## Results and discussion

Synthesis procedures for CNSs are illustrated in Fig. 1a. Pyrolysis of potassium citrate in inert gas results in the formation of 2D CNSs with a hierarchical porous architecture. Involving potassium species is very significant for generating this specific structure. First,  $\text{K}_2\text{CO}_3$  formed at a low-temperature region ( $< 650\text{ }^{\circ}\text{C}$ ) serves as the template for organic species assembly [34, 35]. After pyrolysis and carbonization at elevated temperatures, CNSs with a 2D structure can be formed. In the meantime, the  $\text{CO}_2$  and  $\text{K}_2\text{O}$  produced by the decomposition of  $\text{K}_2\text{CO}_3$  ( $\text{K}_2\text{CO}_3 \rightarrow \text{K}_2\text{O} + \text{CO}_2$ ) can both react with carbon sheets ( $\text{CO}_2 + \text{C} \rightarrow 2\text{CO}$ ,  $\text{K}_2\text{O} + \text{C} \rightarrow 2\text{K} + \text{CO}$ ) at high-temperature [15, 17, 22, 34], making these nanosheets highly porous. This activation process is controllable by annealing temperature, and different porous architectures can be constructed under different temperatures. Potassium citrate is a typical organic–inorganic hybrid with coordinated potassium in its molecule, while organic moiety can be used as a carbon source. This means that the use of potassium citrate for porous carbon preparation can integrate the carbonization and activation processes in only one step, simplifying the production procedure considerably.

Detailed morphology and microstructure of CNSs are characterized by field-emission scanning electron microscopy (FESEM) and transmission electron microscopy (TEM). As shown in Fig. 1b, the CNS-950 exhibits a specific foam-like structure with a large open space inside (the inset). Such a special structure

**Figure 1** **a** Schematic diagram of the synthesis process for CNS-950. **b** FESEM and **c–e** TEM images of the CNS-950.



can effectively buffer mechanical stress of volume variation and sustain the structural integrity of electrode materials. The TEM images verify a foam-like overall structure (Fig. 1c) of CNS-950 constituted by ultrathin carbon nanosheets. These nanosheets are found very porous (Fig. 1d), which contains a large proportion of micropores and mesopores (Fig. 2e). The morphology and structure of CNS-850 and CNS-900 are also characterized by FESEM and TEM test (Fig. S1 and S2), and the 2D CNSs with a highly porous architecture can be maintained.

Crystallinity of these CNSs is characterized using an X-ray diffraction (XRD) test. Two broad peaks at  $2\theta$  near  $23^\circ$  and  $44^\circ$  (Fig. 2a) are typical diffraction peaks of porous carbon with a low graphitization [14, 18, 30]. X-ray photoelectron spectroscopy (XPS) is used to analyze their elemental constitutions and chemical valences. The survey spectra of CNSs

(Fig. S3) show a dominating C 1s peak and a sub-strong O 1s peak, clearly manifesting the existence of C and O atoms. Except for photoelectrons from C–C valence, signals from C–O, and C=O can be positively observed in high-resolution C 1s and O 1s spectra (Fig. 2b, c), indicating residual oxygenated functional groups. Raman spectra (Fig. 2d) show two typical peaks at  $1337$  and  $1596$   $\text{cm}^{-1}$  which represent D and G bands of the  $\text{sp}^3$ -type disordered carbon and  $\text{sp}^2$ -type graphitized carbon, respectively [20, 30, 36]. The D band is from vibrations of C–C bond at the edge of  $\text{sp}^3$  or  $\text{sp}^2$ , which represents the disordered structure of carbon materials. The G band is related to  $\text{sp}^2$  order vibration between the carbon atoms, which corresponds to the tangential vibration of the graphitic layer and carbon atoms. Intensity ratio  $I_G/I_D$  is a common index to evaluate the disorder degree of carbon materials [14, 20, 30]. The  $I_G/I_D$  values of

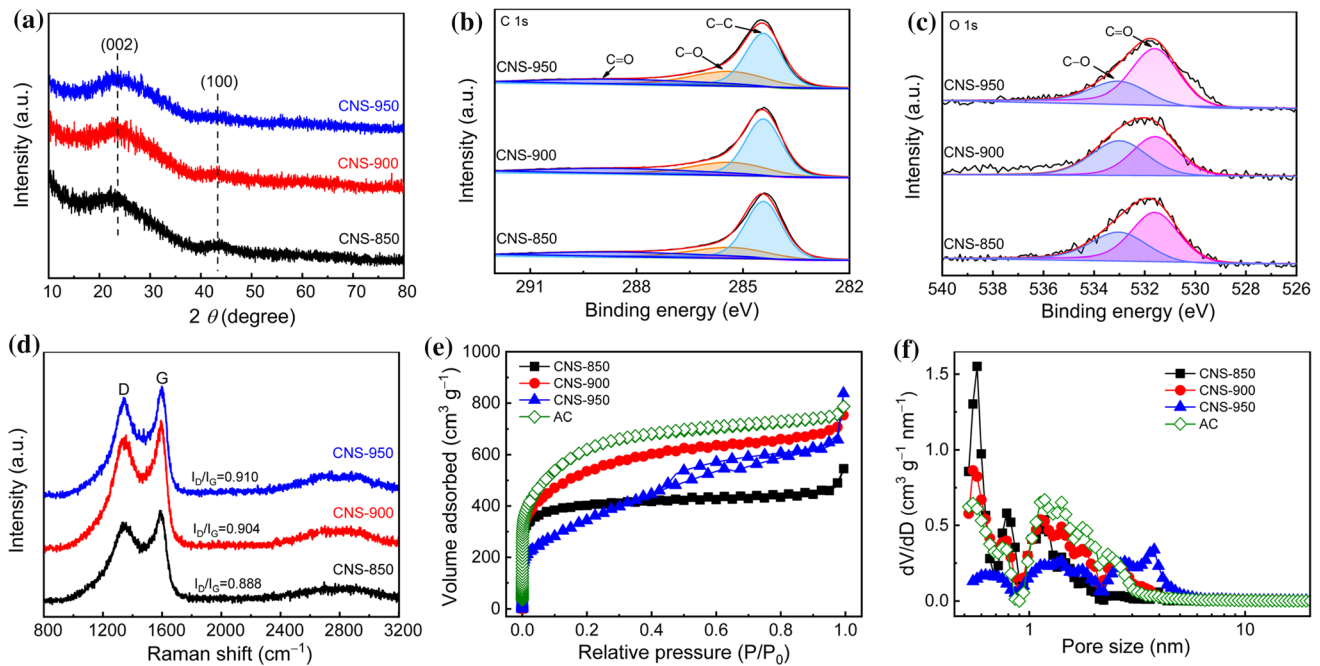


**Figure 2** a XRD patterns, b C 1s XPS spectra, c O 1s XPS spectra, and d Raman spectra of CNS-850, CNS-900 and CNS-950. e  $N_2$  adsorption–desorption isotherms and f pore-size distribution curves of CNS-850, CNS-900, CNS-950 and commercial AC.

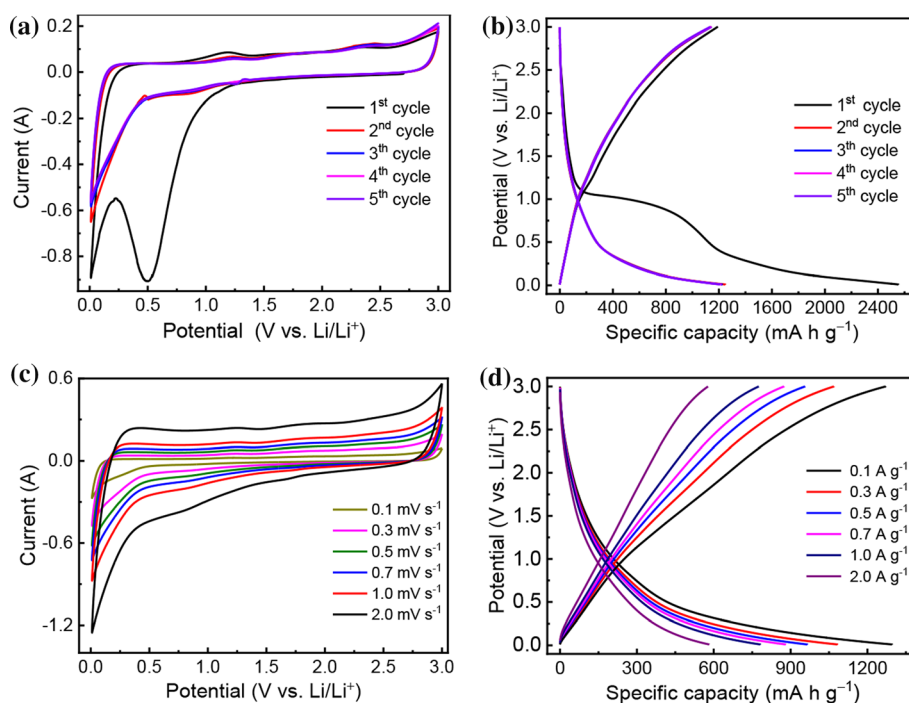
CNS-850, CNS-900 and CNS-950 are 0.888, 0.904 and 0.910, respectively. The results show that the defects and structural deformation in samples increase with the rise of annealing temperature.

$N_2$  adsorption–desorption isotherms are measured to investigate porous structures of CNS samples. Their isotherms can be identified into different types according to the International Union of Pure and Applied Chemistry (IUPAC) classification. As shown in Fig. 2e, the isotherm of CNS-950 belongs to type I and IV owing to the coexistence of mesopores and micropores [14, 18, 37]. Obvious adsorption/desorption hysteresis presented in relative pressure ( $P/P_0$ ) region of 0.5–0.9 demonstrates the existence of mesopores, while  $N_2$  adsorption–desorption at relative pressure lower than 0.1 indicates the presence of micropores. However, the CNS-850 and CNS-900 exhibit comparable adsorption/desorption isotherms as commercial activated carbon (AC), indicating a micropore-dominated porous structure. Barrett-Joyner-Halenda (BJH) pore size distributions in Fig. 2f are calculated from adsorption branches of isotherms, which verify the micropore-dominated porous structures for both CNS-850 and CNS-900, which is very similar to that of commercial AC. Pore size distribution curve of CNS-900 verifies the coexistence of micropores and mesopores in its porous structure.

There is a general trend that CNS samples exhibit reduced micropores and simultaneously enhanced mesopores as the annealing temperature increases. The CNS-950 exhibits a hierarchical porous structure with four size peaks at 0.66, 1.41, 2.77, and 3.79 nm exhibited in its pore size distribution curve. Porous characteristics of CNSs are summarized in Table 1. The CNSs show Brunauer-Emmette-Teller (BET) surface areas of 1539, 1775 and 1061  $m^2 g^{-1}$  for CNS-850, CNS-900, and CNS-950, respectively. Increased BET area of CNS-900 than that of CNS-850 can be attributed to incremental micropores and mesopores in pore size regions of 1–2 and 2–5 nm, respectively. By contrast, reduced micropores lower the BET area of CNS-950, making the sample show the lowest surface area. However, increased mesopores endow the CNS-950 with the largest average pore size and pore volume. Therefore, the activation of CNSs can be affected by adjusting the annealing temperature to further control the pore size distribution. By comparing the porous structure of these CNS samples with that of commercial AC, it is found that these CNS samples all show smaller BET surface area than the commercial AC. However, these CNS samples all exhibit much larger pore volume owing to the specific foam-like structures. The CNS-950 also has a larger average pore size than commercial AC owing

**Table 1** Porous characteristics of CNS samples synthesized at different temperatures

Samples	BET surface area ( $\text{m}^2 \text{g}^{-1}$ )	Total pore volume ( $\text{cm}^3 \text{g}^{-1}$ )	Average pore size (nm)
CNS-850	1536	8.43	0.57
CNS-900	1775	11.65	0.55
CNS-950	1061	12.96	3.79
Commercial AC	1981	1.22	1.18

**Figure 3** Initial five cycles of **a** CV curves at  $0.5 \text{ mV s}^{-1}$  and **b** GCD curves at  $0.1 \text{ A g}^{-1}$ , **c** CV curves at various scan rates from 0.1 to  $5.0 \text{ mV s}^{-1}$ , and **d** GCD curves at a specific current region of  $0.1\text{--}2 \text{ A g}^{-1}$  of CNS-950.

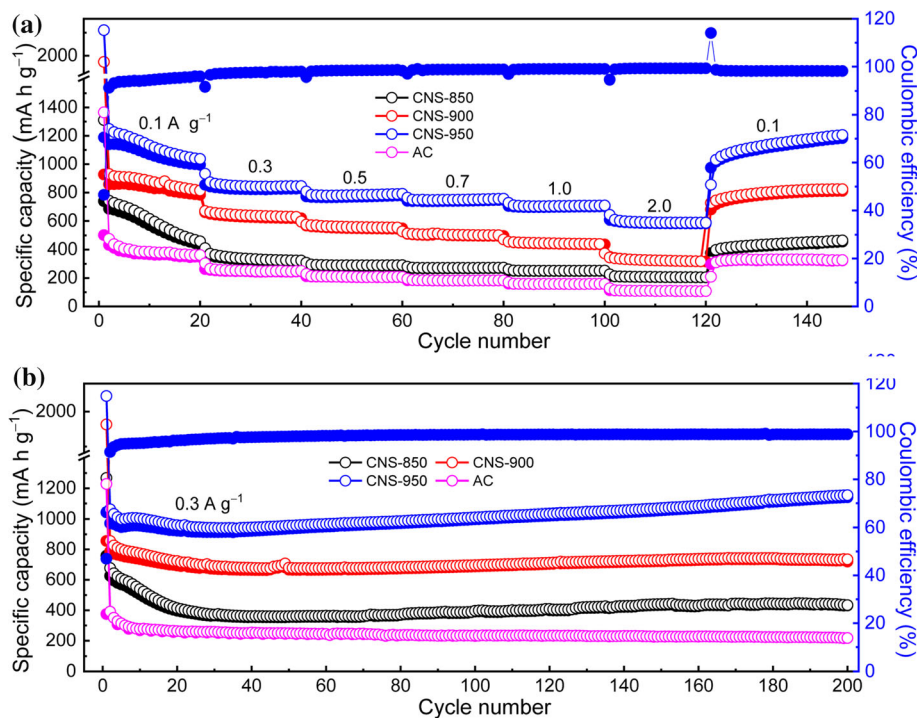
to its mesopores. Therefore, the CNS-950 has the merits of a relative large specific area, huge pore volume and a large average pore size.

These CNSs are used as anode materials in half-cells vs. Li metal to evaluate their performance for Li-ions storage. Figure 3a shows the initial five cycles of CV curves at  $0.5 \text{ mV s}^{-1}$  of CNS-950. It is noted that a different CV curve is demonstrated in the first cycle. A strong cathodic peak around  $0.5 \text{ V}$  is observed in the first cycle while it disappears in subsequent cycles owing to possible irreversible side reactions associated with electrolyte decomposition, solid-electrolyte interface (SEI) formation, and loss of irreversible reaction sites [33, 38, 39]. Notably, CV curves almost overlap after the first cycle, indicating Li-ions storage in CNS-950 is highly reversible and stable in subsequent cycles. Figure 3b exhibits initial 5 cycles of GCD curves at  $0.1 \text{ A g}^{-1}$  of a fresh CNS-950 electrode. In the first delithiation curve, the electrode

shows two plateaus which are typical features of porous carbon electrode [35, 40]. The initial lithiation/delithiation capacity of CNS-950 electrode is  $2554/1189 \text{ mA h g}^{-1}$  with a coulombic efficiency (CE) of 46.5%. Then, the electrode shows a stable capacity higher than  $1130 \text{ mA h g}^{-1}$  in the subsequent cycles. The reversible capacity is about triple the theoretical capacity of graphite ( $372 \text{ mA h g}^{-1}$ ). Figure 3c shows CV curves at different scan rates of CNS-950. These CV curves show a similar shape without any obvious redox peaks. The GCD curves (Fig. 3d) at different rates also show unobvious charge or discharge plateaus. These are typical features of surface-controlled energy storage behavior.

Rate performance of CNS electrodes are compared in Fig. 4a, and in comparison with that of commercial AC electrode. These CNS electrodes all exhibit higher specific capacities at different specific currents than the AC electrode. The CNS-950 shows higher specific

**Figure 4** **a** Rate performances and **b** cycling performance at  $0.3 \text{ A g}^{-1}$  for 200 cycles of CNS-850, CNS-900, CNS-950, and commercial AC.



capacity at different specific currents than CNS-900 and CNS-850. A lithiation/delithiation capacity of  $1248/1140 \text{ mA h g}^{-1}$  at  $0.1 \text{ A g}^{-1}$  is delivered at the 2nd cycle with a CE of 91%, which gradually reduced to  $1037/995 \text{ mA h g}^{-1}$  at the 20th cycle. Then, the CNS-950 shows much stable specific capacity under higher rates. Delithiation capacities around 822, 769, 740, 698, and 586  $\text{mA h g}^{-1}$  is delivered at 0.3, 0.5, 0.7, 1.0, and 2.0  $\text{A g}^{-1}$ , respectively. Even at a high rate of 2.0  $\text{A g}^{-1}$ , the CNS-950 shows 1.57 times the theoretical capacity of graphite, so high capacity is maintained under high rates. When the specific current is returned to 0.1  $\text{A g}^{-1}$ , a lithiation/delithiation capacity of  $1030/1016 \text{ mA h g}^{-1}$  is delivered, which gradually increase with further cycling, and a reversible lithiation/delithiation capacity of  $1206/1184 \text{ mA h g}^{-1}$  is obtained at the 147th cycle. More significantly, as shown in Fig. 4b, the CNS-950 electrode exhibits a long-term cycling stability at 0.3  $\text{A g}^{-1}$ . After slight capacity degradation in initial cycles, the capacity of CNS-950 gradually increases with cycling with CEs around 98%. The electrode maintains 110% of capacity retention after 200 cycles, indicating long-term cycling performance of our CNS-950 electrode. It is found that the CNS samples all exhibit gradually increased specific capacity after initial cycles. The gradually increased capacity during long-term cycling is a common phenomenon of

carbonaceous electrode, which can be ascribed to the activating process from an enlarged interplanar distance, increased edge and surface effects, gradual exfoliation of carbon layers, and increased ion accessibility of small pores [24, 41–43]. However, the CNS-950 shows a faster speed for capacity increasing than CNS-850 and CNS-900. The CNS-950 exhibits the lowest specific area and the sample is more solid than the other CNS samples. Therefore, the activating effect is more apparent and results in faster-increased capacity. The Nyquist plot of electrochemical impedance spectroscopy (EIS) was measured (Fig. S4), and the CNS-950 shows a smaller semicircle at the high-frequency region than both CNS-850 and CNS-900. This result indicates lower charge transfer resistance of CNS-950.

Based on the above analysis, it is found that CNS-950 displays superior performance for Li-ions storage including large specific capacity, excellent rate performance, and long cycle life, which are mainly attributed to the following aspects: first, Li-ions storage in porous carbon is surface-controlled, and accessible surface for electrolyte is very significant to achieve a higher capacity. The CNS samples have a larger pore volume than commercial AC owing to their specific foam-like structure that is constituted by interconnected nanosheets, which can serve as electrolyte reservoirs for better surface utilization;

second, mesopore-enriched structure is another critical factor to promote the performance. Compared to micropores, the mesopores are more effective for Li-ions storage, which promotes the utilization efficiency of surface and accelerates the diffusion speed of ions; third, specific nanosheets structure shortens diffusion paths of Li-ions for fast energy storage.

Practicability of CNS-950 is also evaluated in a full battery assembled with a  $\text{LiNi}_{0.5}\text{Co}_{0.2}\text{Mn}_{0.3}\text{O}_2$  cathode. Capacity of anode and cathode materials are balanced by controlling a mass ratio of 1:8 between CNS-950 and  $\text{LiNi}_{0.5}\text{Co}_{0.2}\text{Mn}_{0.3}\text{O}_2$ , and 100  $\mu\text{L}$  of electrolyte was used in each cell. Owing to the different working potentials of the two electrodes, the full battery displays a maximal voltage of 4.2 V, as verified by the CV (Fig. 5a) and GCD (Fig. 5b) curves. The CV and GCD curves at different rates display a similar shape without apparent redox peaks or

charge/discharge plateaus, which can be ascribed to surface-controlled contributions from CNS-950 anode. The GCD curves under different specific currents all display small IR drop, suggesting high-power performance. Rate performance of the full battery is shown in Fig. 5c. The capacity is calculated referring to the mass of cathode owing to our full battery being cathode limited. A specific capacity around  $170 \text{ mA h g}^{-1}$  is delivered at  $0.1 \text{ A g}^{-1}$  and about  $34 \text{ mA h g}^{-1}$  is maintained at  $2.0 \text{ A g}^{-1}$ . Figure 5d shows Ragone plot of the full battery, where the specific energy and specific power are calculated referring to the total mass of cathode and anode materials. A specific energy of  $319 \text{ W h kg}^{-1}$  is demonstrated at a specific power of  $181 \text{ W kg}^{-1}$ . When the specific power increases to  $2.9 \text{ kW kg}^{-1}$ , a specific energy of  $51 \text{ W h kg}^{-1}$  can be maintained. The energy and power performances are superior to

**Figure 5** **a** CV curves at different scan rates, **b** GCD curves at different specific currents, **c** rate performance and corresponding CE, **d** Ragone plot and its comparison with reported full batteries, and **e** cycling performance and corresponding CE of the CNS-950// $\text{LiNi}_{0.5}\text{Co}_{0.2}\text{Mn}_{0.3}\text{O}_2$  full battery.

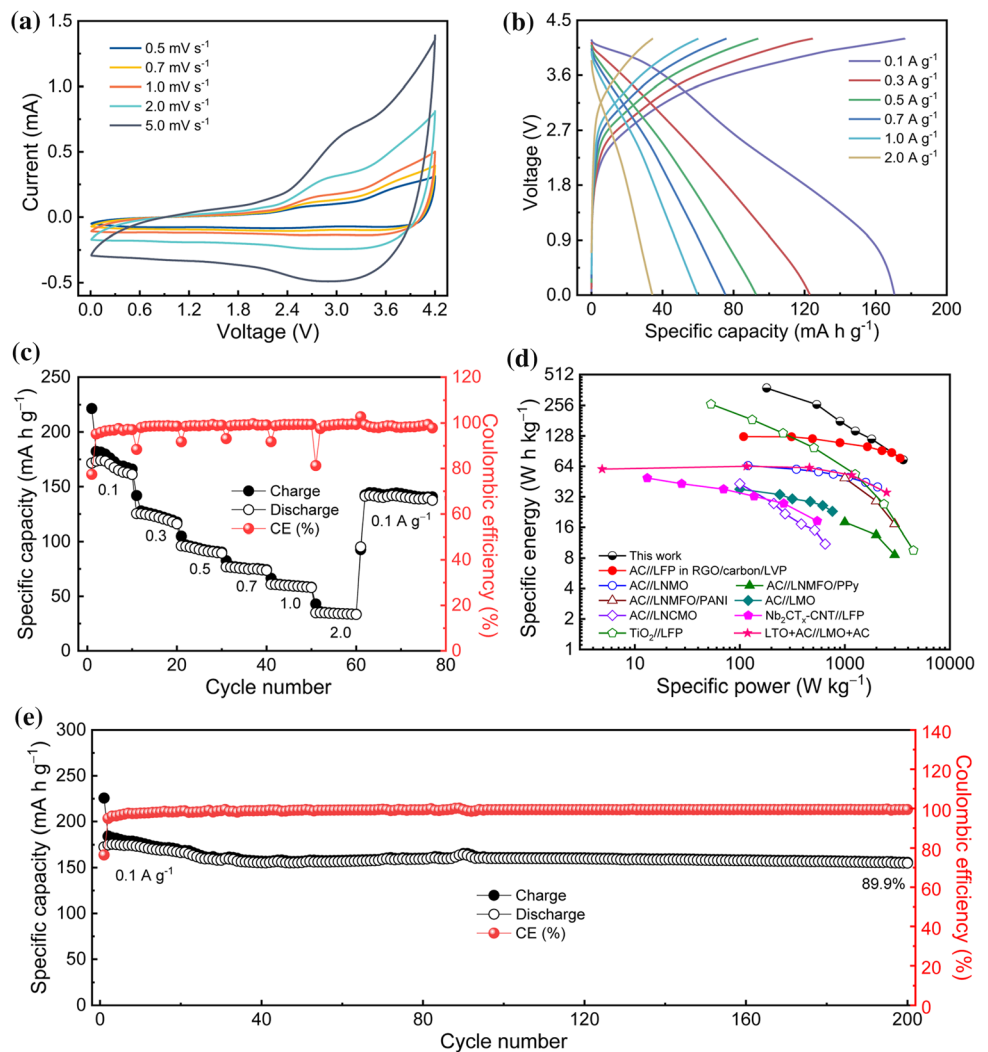




**Table 2** Specific energy and specific power performances of different full batteries reported previously

Types of full batteries	Specific energy (Wh kg <sup>-1</sup> )	Specific power (W kg <sup>-1</sup> )	Ref
CNS-950// LiNi <sub>0.5</sub> Co <sub>0.2</sub> Mn <sub>0.3</sub> O <sub>2</sub>	319.2 (or 50.8)	181.3 (or 2938.1)	This work
AC// LiFePO <sub>4</sub> (LFP) in reduced graphene oxide (RGO)/ carbon/ Li <sub>3</sub> V <sub>2</sub> (PO <sub>4</sub> ) <sub>3</sub> (LVP)	125.76 (or 77)	108.6 (or 3360)	[44]
AC//Li(Ni <sub>0.33</sub> Mn <sub>0.33</sub> Fe <sub>0.33</sub> )O <sub>2</sub> (LNMFO)/ polypyrrole (PPy)	~ 49		[45]
AC//LNMFO/ polyaniline (PANI)	~ 18		[45]
AC//LiMn <sub>2</sub> O <sub>4</sub> (LMO)	38 (or 23)	100 (or 760)	[46]
AC//LiNi <sub>0.33</sub> Co <sub>0.33</sub> Mn <sub>0.33</sub> O <sub>2</sub> (LNCMO)	43 (or 11)	100 (or 650)	[47]
Nb <sub>2</sub> CT <sub>x</sub> /carbon nanotube (CNT)// LFP	49		[48]
TiO <sub>2</sub> // LFP	263		[49]
Li <sub>4</sub> Ti <sub>5</sub> O <sub>12</sub> (LTO) + AC//LMO + AC	60		[50]

the performance of a series of full batteries based on AC [44–47], Nb<sub>2</sub>CT<sub>x</sub> [48], TiO<sub>2</sub> [49], and Li<sub>4</sub>Ti<sub>5</sub>O<sub>12</sub> [50], as shown in Table 2. In addition, the full battery has excellent cycle stability. As shown in Fig. 5e, in a specific current of 0.1 A g<sup>-1</sup>, the full battery has an initial discharged capacity of 172.5 mA h g<sup>-1</sup>. Slightly decreased capacity in the initial 30 cycles can be ascribed to performance coupling between the cathode and anode electrodes. Then, the full battery shows stable capacity in subsequent cycles. A discharge capacity of 155.0 mA h g<sup>-1</sup> is retained at the 200th cycle, corresponding to 89.9% of initial capacity. In the whole cycling process, the full battery shows CEs very close to 100%, indicating a highly reversible reaction in the full battery. These results indicate promising value for practical applications of our CNS samples.

## Conclusions

Mesopore-enrich hierarchical porous carbon nanosheets (CNSs) are directly synthesized by pyrolysis of potassium citrate. The specific 2D structure is formed by the templating effect of potassium salt, and further activation results in a highly porous architecture. Pore sizes of CNSs are tuned by different annealing temperatures, and a hierarchical porous architecture enriched with mesopores can be synthesized at 950 °C (CNS-950). Benefiting the specific 2D structure and mesopore-enriched architecture, the CNS-950 shows increased active sites and shorten ion diffusion distance for Li-ion storage,

resulting in high-capacity, high-rate performances combined with long-term cycling stability. The CNS-950 shows a reversible capacity three times the theoretical capacity of graphite. The CNS-950 also shows excellent performance in full batteries assembled with a commercial cathode. The full batteries demonstrate excellent performance in terms of high-energy, high-power, and long-term cycling performances. This investigation demonstrates the significant role of decreased dimension and enlarged pore size on higher reactivity and faster reaction kinetics, and shows the promising applications of porous carbons in LIBs.

## Acknowledgements

This work is financially supported by the National natural science foundation of China (No. 21905148) and China postdoctoral science foundation (No. 2019T120567 and 2017M612184). The authors also acknowledge the support of the 1000-talents plan, the world-class discipline program, and the Taishan scholars advantageous and distinctive discipline program of Shandong province for supporting the research team of energy storage materials.

## Declarations

**Conflict of interest** The authors declare that they have no conflict of interest.

**Supplementary Information:** The online version contains supplementary material available at <http://doi.org/10.1007/s10853-022-06964-9>.

## References

- [1] Thackeray MM (2020) Exploiting the spinel structure for Li-ion battery applications: a tribute to John B. Goodenough. *Adv Energy Mater* 11:2001117. <https://doi.org/10.1002/aenm.202001117>
- [2] Wu L, Zheng J, Wang L, Xiong X, Shao Y, Wang G, Wang JH, Zhong S, Wu M (2019) PPy-encapsulated SnS<sub>2</sub> nanosheets stabilized by defects on a TiO<sub>2</sub> support as a durable anode material for lithium-ion batteries. *Angew Chem Int Ed* 58(3):811–815. <https://doi.org/10.1002/anie.201811784>
- [3] Qiao L, Wang C, Zhao XS (2021) Encapsulation of iodine in nitrogen-containing porous carbon plate arrays on carbon fiber cloth as a freestanding cathode for lithium-iodine batteries. *ACS Appl Energy Mater* 4(7):7012–7019. <https://doi.org/10.1021/acsaelm.1c01068>
- [4] Miao X, Li H, Wang L, Li Y, Sun D, Zhou X, Lei Z (2020) Monodispersed FeS nanoparticles confined in 3D interconnected carbon nanosheets network as an anode for high-performance lithium-ion batteries. *J Mater Sci* 55:12139–12150. <https://doi.org/10.1007/s10853-020-04843-9>
- [5] Xu J, Dou Y, Wei Z, Ma J, Deng Y, Li Y, Liu H, Dou S (2017) Recent progress in graphite intercalation compounds for rechargeable metal (Li, Na, K, Al)-ion batteries. *Adv Sci* 4(10):1700146. <https://doi.org/10.1002/advs.201700146>
- [6] Roberts AD, Li X, Zhang H (2014) Porous carbon spheres and monoliths: morphology control, pore size tuning and their applications as Li-ion battery anode materials. *Chem Soc Rev* 43(13):4341–4356. <https://doi.org/10.1039/C4CS00071D>
- [7] Zhang J, Xu T, Cong Y, Zhang Y, Li X, Dong Z, Li Y, Yuan G, Zhang J, Cui Z (2019) Improved rate performance and cycling stability of graphitized mesoporous carbon as anode materials for lithium-ion batteries. *J Mater Sci* 54:648–658. <https://doi.org/10.1007/s10853-018-2855-6>
- [8] Shilpa KR, Sharma A (2017) Morphologically tailored activated carbon derived from waste tires as high-performance anode for Li-ion battery. *J Appl Electrochem* 48(1):1–13. <https://doi.org/10.1007/s10800-017-1129-3>
- [9] Zhou H, Zhu S, Hibino M, Honma I, Ichihara M (2003) Lithium storage in ordered mesoporous carbon (CMK-3) with high reversible specific energy capacity and good cycling performance. *Adv Mater* 15(24):2107–2111. <http://doi.org/10.1002/adma.200306125>
- [10] Xu Y, Jiang J, Li Z, Yang Z, Zhang Y, An Y, Zhu Q, Dou ZX (2020) Aerosol-assisted preparation of N-doped hierarchical porous carbon spheres cathodes toward high-stable lithium-ion capacitors. *J Mater Sci* 55:13127–13140. <https://doi.org/10.1007/s10853-020-04955-2>
- [11] Zhao C, Gao H, Chen C, Wu H (2015) Reduction of graphene oxide in Li-ion batteries. *J Mater Chem A* 3(36):18360–18364. <https://doi.org/10.1039/C5TA05068E>
- [12] Wang X, Lv L, Cheng Z, Gao J, Dong L, Hu C, Qu L (2016) High-density monolith of N-doped holey graphene for ultrahigh volumetric capacity of Li-ion batteries. *Adv Energy Mater* 6(6):1502100. <https://doi.org/10.1002/aenm.201502100>
- [13] Kaskhedikar NA, Maier J (2009) Lithium storage in carbon nanostructures. *Adv Mater* 21(25–26):2664–2680. <https://doi.org/10.1002/adma.200901079>
- [14] Niu J, Shao R, Liu M, Liang J, Zhang Z, Dou M, Huang Y, Wang F (2018) Porous carbon electrodes with battery-capacitive storage features for high performance Li-ion capacitors. *Energy Storage Mater* 12:145–152. <https://doi.org/10.1016/j.ensm.2017.12.012>
- [15] Alkarmo W, Ouhib F, Aqil A, Thomassin JM, Vertruyen B, Piedboeuf ML, Job N, Detrembleur C, Jerome C (2018) Continuous-porous N-doped carbon network as high-performance electrode for lithium-ion batteries. *J Mater Sci* 53:6135–6146. <https://doi.org/10.1007/s10853-017-1974-9>
- [16] Kang X, Zhu H, Wang C, Sun K, Yin J (2018) Biomass derived hierarchically porous and heteroatom-doped carbons for supercapacitors. *J Colloid Interface Sci* 509:369–383. <https://doi.org/10.1016/j.jcis.2017.09.013>
- [17] Yin F, Wei XY, Yan WW, Fan ZC, Lu KL, Wei FH, Mao FZ, Zong ZM (2021) Preparation of hierarchical porous carbons from a coal tar pitch modified by fluid catalytic cracking oil for a high-performance supercapacitor. *J Mater Sci* 56:16591–16601. <https://doi.org/10.1007/s10853-021-06317-y>
- [18] Li C, Li J, Zhang Y, Cui X, Lei H, Li G (2019) Heteroatom-doped hierarchically porous carbons derived from cucumber stem as high-performance anodes for sodium-ion batteries. *J Mater Sci* 54:5641–5657. <https://doi.org/10.1007/s10853-018-03229-2>
- [19] Yi Y, Zhao W, Zeng Z, Wei C, Lu C, Shao Y, Guo W, Dou S, Sun J (2020) ZIF-8@ZIF-67-derived nitrogen-doped porous carbon confined CoP polyhedron targeting superior potassium-ion storage. *Small* 16(7):1906566. <https://doi.org/10.1002/smll.201906566>
- [20] Zhou X, Chen L, Zhang W, Wang J, Liu Z, Zeng S, Xu R, Wu Y, Ye S, Feng Y, Cheng X, Peng Z, Li X, Yu Y (2019) Three-dimensional ordered macroporous metal-organic framework single crystal-derived nitrogen-doped hierarchical porous carbon for high-performance potassium-ion

- batteries. *Nano Lett* 19(8):4965–4973. <https://doi.org/10.1021/acs.nanolett.9b01127>
- [21] Fan D, Wei B, Wu R, Zhou J, Zhou C (2021) Dielectric control of ultralight hollow porous carbon spheres and excellent microwave absorbing properties. *J Mater Sci* 56:6830–6844. <https://doi.org/10.1007/s10853-021-05780-x>
- [22] Zhao H, Cheng Y, Liu W, Yang L, Zhang B, Wang LP, Ji G, Xu ZJ (2019) Biomass-derived porous carbon-based nanostructures for microwave absorption. *Nano-Micro Letters* 11(1):24. <https://doi.org/10.1007/s40820-019-0255-3>
- [23] Guo Y, Tan C, Sun J, Li W, Zhang J, Zhao C (2020) Porous activated carbons derived from waste sugarcane bagasse for CO<sub>2</sub> adsorption. *Chem Eng J* 381:122736. <https://doi.org/10.1016/j.cej.2019.122736>
- [24] Liu Y, Shi M, Han M, Yang J, Yu J, Narayanasamy M, Dai K, Angaiah S, Yan C (2020) Spontaneous exfoliation and tailoring derived oxygen-riched porous carbon nanosheets for superior Li<sup>+</sup> storage performance. *Chem Eng J* 387:124104. <https://doi.org/10.1016/j.cej.2020.124104>
- [25] Li Z, Cao L, Chen W, Huang Z, Liu H (2019) Mesh-like carbon nanosheets with high-level nitrogen doping for high-energy dual-carbon lithium-ion capacitors. *Small* 15(15):1805173. <https://doi.org/10.1002/sml.201805173>
- [26] He Y, Zhuang X, Lei C, Lei L, Hou Y, Mai Y, Feng X (2019) Porous carbon nanosheets: synthetic strategies and electrochemical energy related applications. *Nano Today* 24:103–119. <https://doi.org/10.1016/j.nantod.2018.12.004>
- [27] Yu X, Zhan C, Lv R, Bai Y, Lin Y, Huang Z-H, Shen W, Qiu X, Kang F (2015) Ultrahigh-rate and high-density lithium-ion capacitors through hybridizing nitrogen-enriched hierarchical porous carbon cathode with prelithiated microcrystalline graphite anode. *Nano Energy* 15:43–53. <https://doi.org/10.1016/j.nanoen.2015.03.001>
- [28] Han D, Zhang J, Weng Z, Kong D, Tao Y, Ding F, Ruan D, Yang Q-H (2019) Two-dimensional materials for lithium/sodium-ion capacitors. *Mater Today Energy* 11:30–45. <https://doi.org/10.1016/j.mtener.2018.10.013>
- [29] Yun YS, Kim DH, Hong SJ, Park MH, Park YW, Kim BH, Jin HJ, Kang K (2015) Microporous carbon nanosheets with redox-active heteroatoms for pseudocapacitive charge storage. *Nanoscale* 7(37):15051–15058. <https://doi.org/10.1039/C5NR04231C>
- [30] Zhang M, Hu Y, Cheng J, Fu W, Shen Z (2020) Synthesis of highly-ordered two-dimensional hierarchically porous carbon nanosheet stacks as advanced electrode materials for lithium-ion storage. *ACS Appl Energy Mater* 4(1):226–232. <https://doi.org/10.1021/acsaem.0c02166>
- [31] Kesavan T, Sasidharan M (2019) Palm spathe derived N-doped carbon nanosheets as a high performance electrode for Li-ion batteries and supercapacitors. *ACS Sustain Chem Eng* 7:12160–12169. <https://doi.org/10.1021/acssuschemeng.9b01261>
- [32] Gao S, Tang Y, Wang L, Liu L, Sun Z, Wang S, Zhao H, Kong L, Jia D (2018) Coal-based hierarchical porous carbon synthesized with a soluble salt self-assembly-assisted method for high performance supercapacitors and Li-ion batteries. *ACS Sustain Chem Eng* 6(3):3255–3263. <https://doi.org/10.1021/acssuschemeng.7b03421>
- [33] Zheng Z, Zhang X, Pei F, Dai Y, Fang X, Wang T, Zheng N (2015) Hierarchical porous carbon microrods composed of vertically aligned graphene-like nanosheets for Li-ion batteries. *J Mater Chem A* 3(39):19800–19806. <https://doi.org/10.1039/C5TA05183E>
- [34] Sevilla M, Fuertes AB (2014) Direct synthesis of highly porous interconnected carbon nanosheets and their application as highperformance supercapacitors. *ACS Nano* 8:5069–5078. <https://doi.org/10.1021/nn501124h>
- [35] Shi R, Han C, Li H, Xu L, Zhang T, Li J, Lin Z, Wong C-P, Kang F, Li B (2018) NaCl-templated synthesis of hierarchical porous carbon with extremely large specific surface area and improved graphitization degree for high energy density lithium ion capacitors. *J Mater Chem A* 6:17057–17066. <https://doi.org/10.1039/C8TA05853A>
- [36] Xia Q, Yang H, Wang M, Yang M, Guo Q, Wan L, Xia H, Yu Y (2017) High energy and high power lithium-ion capacitors based on boron and nitrogen dual-doped 3D carbon nanofibers as both cathode and anode. *Adv Energy Mater* 7(22):1701336. <https://doi.org/10.1002/aenm.201701336>
- [37] Cao J, Hu Y, Zhu Y, Cao H, Fan M, Huang C, Shu K, He M, Chen HC (2021) Synthesis of mesoporous nickel-cobalt-manganese sulfides as electroactive materials for hybrid supercapacitors. *Chem Eng J* 405:126928. <https://doi.org/10.1016/j.cej.2020.126928>
- [38] Jiang S, Yun S, Cao H, Zhang Z, Feng H, Chen HC (2022) Porous carbon matrix-encapsulated MnO in situ derived from metal-organic frameworks as advanced anode materials for Li-ion capacitors. *Sci China Mater* 65(1):59–68. <https://doi.org/10.1007/s40843-021-1727-3>
- [39] Liao Y, Chen HC, Yang C, Liu R, Peng Z, Cao H, Wang K (2022) Unveiling performance evolution mechanisms of MnO<sub>2</sub> polymorphs for durable aqueous zinc-ion batteries. *Energy Storage Mater* 44:508–516. <https://doi.org/10.1016/j.ensm.2021.10.039>
- [40] Samdani JS, Tran TN, Kang TH, Lee BJ, Jang YH, Yu JS, Shanmugam S (2021) The identification of specific N-configuration responsible for Li-ion storage in N-doped porous carbon nanofibers: an ex-situ study. *J Power Sources* 483:229174. <https://doi.org/10.1016/j.jpowsour.2020.229174>

- [41] Hu J, Xu Z, Li X, Liang S, Chen Y, Lyu L, Yao H, Lu Z, Zhou L (2020) Partially graphitic hierarchical porous carbon nanofiber for high performance supercapacitors and lithium ion batteries. *J Power Sources* 462:228098. <https://doi.org/10.1016/j.jpowsour.2020.228098>
- [42] Zheng Z, Zhang X, Pei F, Dai Y, Fang X, Wang T, Zheng N (2015) Hierarchical porous carbon microrods composed of vertically aligned graphene-like nanosheets for Li-ion batteries. *J Mater Chem A* 3:19800–19806. <https://doi.org/10.1039/C5TA05183E>
- [43] Kim DW, Jung SM, Senthil C, Kim SS, Ju BK, Jung HY (2021) Understanding excess Li storage beyond  $\text{LiC}_6$  in reduced dimensional scale graphene. *ACS Nano* 15:797–808. <https://doi.org/10.1021/acsnano.0c07173>
- [44] Zhang Y, Zhang Z, Tang Y, Jia D, Huang Y, Pang W, Guo Z, Zhou Z (2019)  $\text{LiFePO}_4$  particles embedded in fast bifunctional conductor  $\text{rGO}\&\text{C}@ \text{Li}_3\text{V}_2(\text{PO}_4)_3$  nanosheets as cathodes for high-performance Li-ion hybrid capacitors. *Adv Funct Mater* 29(17):1807895. <https://doi.org/10.1002/adfm.201807895>
- [45] Brandt A, Balducci A, Rodehorst U, Menne S, Bhaskar A (2014) Investigations about the use and the Degradation mechanism of  $\text{LiNi}_{0.5}\text{Mn}_{1.5}\text{O}_4$  in a high power LIC. *J Electrochem Soc* 161:A1139–A1143. <https://doi.org/10.1149/2.105406jes>
- [46] Karthikeyan K, Amaresh S, Aravindan V, Kim H, Kang KS, Lee YS (2013) Unveiling organic–inorganic hybrids as a cathode material for high performance lithium-ion capacitors. *J Mater Chem A* 1(3):707–714. <https://doi.org/10.1039/C2TA00553K>
- [47] Wang Y, Luo J, Wang C, Xia Y (2006) Hybrid aqueous energy storage cells using activated carbon and lithium-ion intercalated compounds. *J Electrochem Soc* 153:A1425–A1431. <https://doi.org/10.1149/1.2203772>
- [48] Byeon A, Glushenkov AM, Anasori B, Urbankowski P, Li J, Byles BW, Blake B, Van Aken KL, Kota S, Pomerantseva E, Lee JW, Chen Y, Gogotsi Y (2016) Lithium-ion capacitors with 2D  $\text{Nb}_2\text{CT}_x$  (MXene)-carbon nanotube electrodes. *J Power Sources* 326:686–694. <https://doi.org/10.1016/j.jpowsour.2016.03.066>
- [49] Choi D, Wang D, Viswanathan VV, Bae IT, Wang W, Nie Z, Zhang JG, Graff GL, Liu J, Yang Z, Duong T (2010) Li-ion batteries from  $\text{LiFePO}_4$  cathode and anatase/graphene composite anode for stationary energy storage. *Electrochem Commun* 12(3):378–381. <https://doi.org/10.1016/j.elecom.2009.12.039>
- [50] Ruan D, Huang Y, Li L, Yuan J, Qiao Z (2017) A  $\text{Li}_4\text{Ti}_5\text{O}_{12} + \text{AC}/\text{LiMn}_2\text{O}_4 + \text{AC}$  hybrid battery capacitor with good cycle performance. *J Alloys Compd* 695:1685–1690. <https://doi.org/10.1016/j.jallcom.2016.10.318>

**Publisher's Note** Springer Nature remains neutral with regard to jurisdictional claims in published maps and institutional affiliations.